Plasmon enhanced Raman from Ag nanopatterns made using periodically poled lithium niobate and periodically proton exchanged template methods

Signe Damm[1], N. Craig Carville[1], Brian J. Rodriguez[1], Michele Manzo[2], Katia Gallo[2], James H. Rice[1]

[1] School of Physics, University College Dublin, Belfield, Dublin 4, Ireland.
[2] Department of Applied Physics, Laser Physics, Royal Institute of Technology, Roslagstullbacken 21, 106 91 Stockholm, Sweden

KEYWORDS. ferroelectric lithography, SERS, periodically poled lithium niobate, periodically proton exchanged

ABSTRACT. We study Ag nanopattern arrays formed using Ferroelectric lithography based on two separate approaches i.e. periodically poled lithium niobate (PPLN) and periodically proton exchanged (PPE) template methods. We demonstrate that such nanoarrays are plasmon active. Raman spectroscopy was applied to study a molecular probe 4-Aminothiophenol (4-ABT) absorbed onto a silver nanostructured array. The observed Raman spectra show peaks arising from b_2 modes, which occur for plasmon enhanced Raman from 4-ABT in place of a_1 modes, which occur in normal Raman scattering. We demonstrate that

the PPLN and PPE substrates possess different plasmonic properties with PPE creating a stronger SERS signal relative to PPLN substrates.

Self-assembly facilitates the association of atomic and molecular structures into larger structural architectures, which possess nanoscale sized features that incorporate a high degree of functionality [1,2]. This approach has been applied to produce a wide range of nanomaterials, including low dimensional quantum dots and quantum wires [3-5]. A main focus on nanopattern research has centred on assembling pre-defined and pre-synthesized tubes and wires with theoretically predicted properties into a technologically feasible environment. One approach that can be used to create pre-defined arrays of nanopatterns is via directed self-assembly [6]. Directed self-assembly employs the basic principles of self-assembly by carefully choosing the building blocks and facilitating the process by modulating the thermodynamic forces to create ordered assemblies. One approach to achieve this is to organise particles with specific physical properties via external directing fields such as electric fields.

Metallic nanostructures made from ‘coinage’ metals such as silver or gold, yield plasmons when light creates a collective oscillation of the conduction electrons on the surface of the metal [7-9]. Plasmons occur when light at wavelengths resonant with electron oscillations occur, creating a greatly enhanced electromagnetic field. The specific properties of the plasmonic structures have been found to be greatly dependent on factors such as size, shape, and dielectric environment [7-9]. These properties have been exploited in a variety of plasmonic applications ranging from sensing to enhanced fluorescence [2].

Lithography-based methods are widely applied to create metallic nanostructures. While such methods as e-beam lithography create high quality arrays of nanostructures, they can be

expensive and time-consuming. Ferroelectric lithography is an emerging method that enables directed self-assembly that potentially offers a cost effective way to create arrays of metallic nanostructures [6,10]. This approach has the potential to enable control of surface assembly processes with nanoscale precision over large lateral sample sizes, for example, millimetre to centimetre. Ferroelectric materials have a spontaneous polarization, the direction of which can be switched between stable states under an applied electric field greater than the coercive field. This results in the presence of spatially distributed patterns with different surface reactivities. The polarization can be controlled spatially to <10 nm using methods such as atomic force microscopy (AFM). These properties potentially enable domain structured ferroelectrics to act as templates for the assembly of various functional nanostructures.

Ferroelectric lithography-based methods have been applied to direct self-assembly of silver nanoparticles to form a number of different nano and microstructured materials [6, 10-15]. Studies have showed that metallic nanoparticle deposition from an aqueous solution onto +Z surfaces of $LiNbO_3$ domain patterns can be achieved [10-12]. The nanopatterned features created using Ag nanoparticles possessed a uniform distribution with a size variation between 2–10 nm in both diameter and height [11]. Under certain conditions during the photochemical reduction reaction of Ag^+ to Ag^0 on $LiNbO_3$ has been shown to form nanostructures along domain walls [16], and have further been shown to be conducting [17]. Dunn and Tiwari have demonstrated photochemical reduction on both +Z and -Z surfaces, and have demonstrated that the power of the irradiation is a critical parameter [19]. Sun et al. have further reported on the dependence of the wavelength of the light and of the concentration of the solution [20].

Ferroelectric lithography potentially offers a method to create substrates that support reproducible surface enhanced Raman spectroscopy via arrays of nanopatterns made from

silver nanoparticles [21]. While a number of studies have shown that a range of metallic nano and micro structures can be made using ferroelectric lithography few studies have been performed applying such structures to surface enhanced Raman spectroscopy. Here, we apply ferroelectric lithography to create plasmon-active nano- and micro-structures. The Ag nanopattern arrays were made in two ways (using periodically poled lithium niobate (PPLN) and periodically proton exchanged (PPE) templates). We study their plasmonic activity via Raman spectroscopy in combination with finite element analysis.

The Ag nanopattern arrays were made using PPLN and PPE templates. The methodology to create the nanopattern arrays is shown schematically in Figure 1a. A 2D cross-sectional structure of a commercially available PPLN (Crystal Technology Inc.) is shown in Figure 1a-i. The schematic shows the approach taken to create patterned arrays of ferroelectric domains by periodic poling. An electric field exceeding the coercive value of $LiNbO_3$ is applied to an originally monodomain $LiNbO_3$ substrate (purple) by periodic electrodes (black), separated by insulating material acting as a mask (pink blocks). This results in a periodic polarisation reversal of the substrate, following the electrode pattern. After removal of the insulating material and the electrodes, the photodeposition experiments were carried out.

The fabrication process of the PPE samples is illustrated by Figure 1a-ii. The surface of a congruent $LiNbO_3$ sample is first covered with a periodic Ti-mask [patterned via photolithography and reactive ion etching (RIE)] and then immersed in a proton-rich benzoic acid melt. The surface regions of $LiNbO_3$ exposed to the acidic melt undergo a proton-exchange process, whereby Li+ ions of the crystalline lattice are replaced with H^+ coming from the proton source. During this process there is also some lateral diffusion of the protons inside the crystal, under the titanium mask. Two different masks were used to create two different silver structures, referred to PPE and Hex-PPE. PPE samples consist of a 6 μm

periodic pattern. It consists of a central PE region (2.6μm) and two lateral diffusion (LD) regions (each 1.5 μm), with $LiNbO_3$ (0.5 μm) separating one PE + LD structure from the next, as illustrated as inset in figure. 1d. A proton exchange sample was made up of 6 sizes of a Hex-PPE structure divided into a 2D grid (2 rows, 3 columns), with each grid cell consisting of 15 (3 rows, 5 columns) Hex-PPE structures of same size, between 10 to 300 μm. In this paper a 30 μm Hex-PPE structure was used. After proton exchange, the Ti mask is removed by a quick etch (few seconds) in a 40% HF-H_2O solution.

The silver is deposited by photochemical reduction under UV irradiation along the boundaries between ferroelectric domains of the substrate (see figure. 1a-i and 1a-ii) where the electric field magnitude is at maximum, creating nanopatterned arrays along the x-axis. The samples were cleaned prior to deposition of silver by sonication for 20 minutes each in isopropanol, acetone, and Milli-Q water. After 150 μl of 10^{-2} M concentration $AgNO_3$ solution was pipetted onto the surface of the samples. The samples were illuminated with a Spectroline 254 nm wavelength penlamp at a distance of 2 cm above the surface for 10 minutes. The 254 nm wavelength has a higher energy than the bandgap of $LiNbO_3$ (>3.9 eV), creating photogenerated charge which can partake in oxidation and reduction reactions. The photogenerated electrons results in selective deposition of Ag particles on the ferroelectric template through a reduction reaction [16]. The sample was subsequently immersed in Milli-Q water for 1 minute and blown dry with compressed nitrogen. On PPE samples, we obtained a preferential deposition of silver on the crystal surface at the LD – $LiNbO_3$ boundaries and on the neighbouring LD regions [21]. RIE method (reactive ion etching) used for the PPE patterning in the TI-mask may be the cause of a special silver deposition at the edges of the sample. The properties responsible are still unknown but it is believed that the Cl-ions used for etching have been trapped in this region, creating thin lines of strong electric field where

silver has been able to deposit [21]. These silver nanopatterns are referred to RIE-PPE and are 300 nm wide and up to 7 nm high, similar to the PPLN nanopattern.

Raman spectroscopy was performed using a bespoke optical microscope system with an EMCCD and scanning stage attached. A 50x objective was used in epi-fluorescence excitation and collection of the dispersed Raman scattered light. Three excitation wavelengths were available, 473, 532 and 632 nm. AFM measurements were undertaken using an Asylum Research MFP-3D AFM system in intermittent contact mode and PPP-NCH (MikroMasch, 330 kHz resonant frequency and 42 N/m spring constant) cantilevers.

Studies were undertaken to make and characterise Ag nanopatterned arrays using PPLN and PPE templates. Figure. 1b shows a linear feature on the PPLN sample with dimensions of 200 nm in width and an average of 10 nm in height. This feature is attributed to the directed self-assembled Ag nanoparticles, forming a linear periodic pattern, referred to as a nanopattern. The amount and height of the silver deposition can be controlled by varying the concentration of the $AgNO_3$ solution. These images show a silver nanopattern made with a low concentration 10^{-5} M $AgNO_3$, since at this concentration the sample has well defined linear periodic patterns. The PPLN samples used for Raman studies in this paper have been made with a higher concentration, 10^{-2} M $AgNO_3$, giving an average nanopattern height up to 20 nm. The silver nanopatterns are microns in length and are paired at their ends (corresponding to the boundaries of poled domains). Figure 1b insert shows the PPLN nanopattern, showing the paired nanopattern and is marked to show the +Z and –Z poled surfaces. The paired nanopatterns are spaced 14 μm apart. Figure 1c shows a zoomed in image showing the nanopatterns of silver nanoparticles. The nanopattern features repeat across the substrate to form an array pattern across the sample, which matches the template pattern. Figure 1d is an AFM topography image showing the nanopattern of silver nanoparticles on a PPE sample. As

marked on the image, the dark areas, approximately 1 μm-wide, correspond to unexchanged $LiNbO_3$. The light areas, approximately 1.5 μm-wide, was the lateral diffusion region where the silver nanoparticles deposited and the areas between these structures, approximately 2 μm-wide, are the PE regions. A monolayer of Aminothiophenol (4-ABT) was prepared by dipping the samples in 2 mM 4-ABT MeOH solution for 15 min., following 5 min. in MeOH to wash off any excess 4-ABT molecules.

Raman spectroscopy of the PPLN sample was performed as outlined in Figure 2a and b. Raman spectroscopy of the $LiNbO_3$ + 4-ABT was performed were the substrate was poled (using the same procedure applied to prepare the substrate for assemble of Ag) the resulting Raman spectrum shown in Figure 2a-i. The Raman spectrum shows several strong Raman bands, seen up to c.a. 1000 cm^{-1}, thereafter no Raman bands occur. Supplementary information S1 outlines the observed Raman from PPLN in the region > 1000 cm^{-1} for $LiNbO_3$ with 4-ABT were Ag nanopatterns are present and with no Ag, no Raman bands are observed in this spectral region in the absence of Ag. The Raman spectrum for $LiNbO_3$ [22] matches all the observed spectral features. Raman studies were then undertaken on the system: $LiNbO_3$ + Ag nanopattern + 4-ABT. The Raman spectrum was recorded (see Figure 2a-ii) by placing the excitation laser over a metallic region with the 4-ABT molecule present. Strong bands were seen both below and above 1000 cm^{-1}, The Raman spectrum in Figure 2a-ii (displaying only the region above 1000 cm^{-1}) shows several strong bands, whose spectral features can be assigned to 4-ABT [22,23]. Figure 2b-i and Figure 2b-ii show the Raman spectrum of 4-ABT obtained from the Ag nanopattern array (attributed to surface enhanced Raman of 4-ABT, see below) along with the Raman spectrum of 4-ABT powders. The inset in Figure 2b shows the Raman spectrum of 4-ABT using two different excitation wavelengths, i) λ=633 nm and ii) λ=532 nm.

The Raman spectra from 4-ABT recorded as a powder show a series of bands, outlined in table 1, the positions and relative intensities of which are in agreement with literature reports for normal Raman scattering from 4-ABT [23]. The major peaks in the Raman spectrum of 4-ABT powders (table 1) are assigned to a_1 type vibrations. The Raman spectrum of 4-ABT powders shows two strongly intense bands in contrast to the Raman spectrum of 4-ABT + Ag nanopattern arrays, which possess five strongly intense bands. The latter are assigned to a combination of a- and b- type vibrational symmetries [23]. Assignments of four of the five most intense bands (i.e. bands at 1146, 1393, 1437, and 1580 cm^{-1}) can be attributed to b_2 vibrations as outlined in table 1. The band at 1076 cm^{-1} can be assigned to a_1 type. These spectral features have been previously observed and assigned to surface enhanced Raman i.e. the Raman features that occur in the presence of Ag resulting in plasmon or surface enhanced Raman. When plasmon enhanced Raman scattering occurs, the Raman scattering spectral profile of 4-ABT undergoes a change in enhancing b_2 modes. Reports as to the origin of differences between the surface enhanced Raman and normal Raman for 4-ABT have been made suggesting that the b-type surface enhanced Raman bands are intrinsic to 4-ABT itself appearing in conjunction with the chemical enhancement mechanism in plasmon enhanced Raman i.e. that the four non-totally symmetric b_2 modes are selectively enhanced in surface enhanced Raman via a Herzberg-Teller (vibronic) term [23]. However, Wu et. al. theoretically showed that the additional peaks were not due to an enhancement via a Herzberg-Teller (vibronic) term but instead they proposed that the spectral differences originated from a photoreaction of 4-ABT forming p,p′-dimercaptoazobenzene (DMAB) on Ag with the nanoscale roughened Ag surface acting as a catalyst [24]. The b_2 vibrations from 4-ABT were assigned to the N=N and C-N stretching vibrational modes of DMAB. Fang et. al. further assigned the peaks around 1432 and 1390 cm^{-1} to the N=N vibrational modes and the peak around 1143 cm^{-1} to the C-N vibrational mode [25]. The strong Raman peak at 1580

cm^{-1} may give an indication of the amount of DMAB present relative to 4-ABT. The peak from 4-ABT at 1598 cm^{-1} is weak interpreted to arise from a combination of the peak at 1595 cm^{-1} from 4-ABT and the peak at 1575 cm^{-1} from DMAB where most of the 4-ABT has been transformed to DMAB by photoreaction on the silver nanopatterns [26]. As discussed by Huang et. al., this may indicate that both molecules were present on the silver nanopatterns [26].

Figure. 2c and d shows the results obtained from the PPE sample prepared with silver and the probe molecule 4-ABT at different positions on the sample. The Raman signal from the system PPE $LiNbO_3$ + Ag + 4-ABT in figure. 2c-i shows a big enhancement of the Raman signal from 4-ABT (apparent at wavenumbers > 1000 cm^{-1}), while the measurement from PPE $LiNbO_3$ + 4-ABT in figure. 2c (curve iii) shows no Raman signal from 4-ABT. The Raman signal from $LiNbO_3$ is different from the surface and the bulk (see supplementary information S2). Raman signal from $LiNbO_3$ at the surface of the sample shows an additional peak at 617 cm^{-1} compared to the Raman signal from $LiNbO_3$ in the bulk. The Raman signal from bulk $LiNbO_3$ is shown in figure. 2a-i and part of the Raman signal from surface $LiNbO_3$ in figure. 2c-i and 2c-ii. No differences were seen below 617 cm^{-1}. The Raman signals in figure. 2c demonstrates the importance of Ag to enhance the Raman signal from 4-ABT. The RIE-PPE region of the sample produced Raman signal (as outlined in supplementary information S3) arising from some Ag deposition in this region. S3 shows an AFM image of the RIE and PPE pattern at the edge of the PPE sample showing that silver deposition in the RIE region can occur. This nanopattern enhance the Raman signal from 4-ABT as shown in figure. 2c-ii. Figure. 2d shows the Raman signal from 4-ABT on PPE obtained using 3 different excitation wavelengths, λ_{ex} = 532 nm (green graph), λ_{ex} = 633 nm (red graph) and λ_{ex} = 473 nm (blue graph). The strong Raman spectra obtained for 4-ABT on the PPLN, PPE and RIE-PPE nanopattern array possess spectral features that was assigned to surface

enhanced Raman of the probe molecule by Ag present as nanopattern arrays. This indicates that the Ag nanopattern array structure supports surface plasmon polaritons with 473 nm, 532 nm and 633 nm excitation.

A study of Raman signal intensity as a function of position on a PPE-Hex nanopatterned structure was undertaken. Micro-sized hexagonal shaped structures (shown in Figure 3a) were made with Ag assembled at the edges of the structure only. The distance between the edges was measured to be 30 micons. Studies were was undertaken to demonstrate that the observed enhanced Raman signal originates at places where silver deposition occurs. The laser was moved across the silver hexagonal PPE regions to show the spatial dependence of the Raman signal from the probe molecule. A plot of Raman intensity vs. distance was recorded as the excitation laser is brought across a hexagonal structure. Figure 3b shows a plot of Raman signal vs. distance obtained at the b_2 band (at 1160 cm^{-1}). Significantly increased Raman signal intensity is seen at the locations of the silver deposition at the domain boundaries.

An AFM topography image of the domain boundary shown in figure. 3c shows that the width of the silver deposition is c.a. 2 μm. The Raman signal in both figure 3b is broad compared to the width of the silver deposition (2 μm). This is due to the size of the laser spot which is measured to be around 15 μm. Figure 3d shows a plot of Raman signal from the b_2 band at 1437 cm^{-1} when the laser is brought across an area of high enhanced Raman signal. An examination of the Raman intensity in Figure 3b and 3d shows a variation in Raman intensities at each of the edges for the b_2 bands at 1160 and 1437 cm^{-1}, respectively. These variations were as a percentage < 5 per cent and < 21 per cent of the overall signal level, respectively. Signal reproducibility can potentially be further improved using such structures

via, improvements in sample preparation such as improved control over the deposition of the nanoparticles onto the substrate potentially improves this reproducibility.

Calculation of the electric field distribution at the silver-air interface was done via COMSOL by finite element analysis using RF module and excitation using background field of 1 V/m in field strength. The modelled structure was made directly from the AFM line profile of the silver nanopattern from Figure 1a (see also supplementary information S4). The calculations were made in 2D with an electromagnetic (EM) wave incident on the silver from below with an electric field polarized along the nanopattern array. The wave was modified in COMSOL using the build in dielectric properties of $LiNbO_3$ at excitation wavelength and crystal orientation, since the wave travels through $LiNbO_3$ before reaching the silver structures. The silver is defined by its dielectric properties obtained from Johnson and Christy [27]. The results are displayed in Figure 4 and 5, respectively.

Figure. 4a and 5a shows the average electric field enhancement at excitation wavelengths between 450 and 710 nm, for PPLN and PPE nanopattern respectively. The average electric field was calculated from points along the silver surface. Figure 4b-d and 5b-d show the electric field distribution along the silver surfaces for the PPLN and PPE nanopattern respectively. The AFM line profiles used are shown as insets in figure. 4b and 5b for the PPLN and PPE sample respectively (see supplementary information for more details). Results was extracted at wavelengths where the Raman signal from 4-ABT was measured for the three excitation wavelengths, λ_{ext}=473 nm, λ_{ext}=532 nm and λ_{ext}=633 nm. Calculations on the PPLN nanopattern shows that excitation wavelength in the blue causes the highest enhancement while excitation in the red, causes a relatively low enhancement. Experimentally it has only been possible to measure the enhancement using, λ_{ext}=532 nm and λ_{ext}=633 nm, which show that the quality of the Raman signal from 4-ABT was best when

using λ_{ext}=532 nm. Calculations on the PPE nanopattern show the same tendency in wavelength dependence. The blue excitation wavelength causes the highest enhancement while excitation in the red, causes a low enhancement. The difference is very low and may not be representative for the whole sample since the silver deposition is somewhat random in surface topography. Experimentally, at λ_{ext} = 532 nm the Raman signal from 4-ABT is of best quality, with the Raman signal from λ_{ext} = 633 nm showing a good enhancement as well. λ_{ext} = 473 nm shows a weaker enhancement but still of good quality as shown in figure. 2d. Supplementary information S5 shows Raman spectra of $LiNbO_3$ and 4-ABT at different excitation wavelengths, different Raman relative intensities are observed. This difference between experimental and calculation Raman intensities can be potentially explained by referring to other effects physical effects that may play a role in addition to plasmonic effects. Effects such as photorefractive effects in the $LiNbO_3$ substrate yielding a build-up of charges and also changes in refractive index can affect the resulting SERS signal via for example distorting the spot size thereby affecting the SERS intensity distribution.

The AFM line profiles of the silver structure show a more irregular silver deposition on the PPLN sample compared to PPE sample, i.e. more free space vs. Ag nanoparticles exist on the PPLN sample while the Ag nanoparticles on the PPE sample are more closely packed. Greater surface irregularity causes a greater electric field enhancement as calculated. Finite element analysis calculations indicate that the Ag nanopattern structure supports locally electric field strengths up to 5 V/m, using the PPE samples and up to 35 V/m using the PPLN sample.

In conclusion, we have studied Ag nanopattern arrays formed using Ferroelectric lithography based on two separate approaches, specifically periodically poled lithium niobate (PPLN) and periodically proton exchanged (PPE) template methods. We demonstrate that such

nanoarrays are plasmon active. Raman spectroscopy was applied to study a molecular probe 4-Aminothiophenol (4-ABT) absorbed onto a silver nanostructured array. The observed Raman spectra show peaks arising from b_2 modes, which occur for plasmon enhanced Raman (ie SERS) from 4-ABT in place of a_1 modes, which occur in normal Raman scattering. We demonstrate that the PPLN and PPE substrates possess different plasmonic properties with PPE creating a stronger SERS signal relative to PPLN substrates.

Associated Content

Supporting Information

Supplementary information outlines additional information in regard to the SERS from the nanopatterned array substrates in addition to the substrates Raman spectrum. Information pertaining to the AFM imaging of the substrates and calculations are also outlined. This material is available free of charge via the Internet at http://pubs.acs.org

Author information

Corresponding author
James Rice,
School of Physics, University College Dublin,
Belfield, Dublin 4, Ireland.
Email: james.rice@ucd.ie
Phone: 00353 17172229

Acknowledgments

The authors would like to acknowledge Science Foundation Ireland for their support of this this research. The work was partially supported through the DGPP funded under the Programme for Research in Third Level Institutions (PRTLI) Cycle 5 and the European Regional Development Fund.

References

1. Zhao, X.; Pan, F.; Xu, H.; Yaseen, M.; Shan, H.; Hauser, C.A.E.; Zang, S.; Lu, J.R.; Chem. Soc. Rev. 2010, 39, 3480-3489.

2. Huie, J.C.; Smart Materials and Structures, 2010, 12, 264.

3. Taylor, R.A.; Robinson, J.W.; Rice, J.H.; Jarjour, A.; Smith, J.D.; Oliver, R.A.; Briggs, G.A.D.; Kappers, M.J.; Humphreys, C.J.; Arakawa, Y.; Phys. E-Low D. Syst. Nano., 2004, 21, 285-289.

4. Na, J.H.; Taylor, R.A.; Rice, J.H.; Robinson, J.W.; Lee, K.H.; Park, Y.S.; Park, C.M.; Kang, T.M.; Appl. Phys. Lett., 2005, 86, 083109.

5. Qian, L.; Mookherjee, R.; Nano Res., 2011, 4, 1117-1120.

6. Li, D.; Bonnell, D.A.; Annu. Rev. Mater. Res. 2008, 38, 351-360.

7. Lordan, F.; Rice, J.H.; Jose, B.; Forster, R.J.; Keyes, T.E.; Appl. Phys. Lett. 2010, 97, 153110-153113.

8. Lordan, F.; Rice, J.H.; Jose, B.; Forster, R.J.; Keyes, T.E.; Appl. Phys. Lett. 2011, 99 033104-033107.

9. Lordan, F.; Rice, J.H.; Jose, B.; Forster, R.J.; Keyes, T.E.; J. Phys. Chem. C, 2012, 116, 1784-1789.

10. Liu, X.; Hatano, H.; Takekawa, S.; Ohuchi, F.; Kitamura, K.; Appl. Phys. Lett. 2011, 99, 053102-053105.

11. Liu, X.; Kitamura, K.; Terabe, K.; Hatano, H.; Ohashi, N.; Appl. Phys. Lett. 2007, 91, 044101-044104.

12. Shen, Z.; Chen, G.; Chen, Z.; Qu, X.; Chen, Y.; Liu, R.; Langmuir, 2011, 27 5167-5172.

13. Shen, Z.; Qu, X.; Chen, Y.; Liu, R.; ACS Nano, 2011, 5, 6855–6860.

14. Giocondi, J.L.; Rohrer, G.S.; Chem. Mater., 2001, 13, 241–242.

15. Burbure, N.V.; Salvador, P.A.; Rohrer, G.S.; Chem. Mater., 2010, 22 5831-5837.

16. Hanson, J.N.; Rodriguez, B.J.; Nemanich, R.J.; Gruverman, A.; Nanotechnology, 2006, 17, 4946-4951.

17. Haussmann, A.; Milde, P.; Erler, C.; Eng, L.M.; Nano Letters, 2009, 9, 763-768.

18. Whitney, T.M.; Jiang, J.S.; Searson, P.C.; Chien, C.L.; Science 1993, 261, 1316-1320.

19. Dunn, S.; Tiwari, D.; Appl. Phys. Lett. 2008, 93, 092905-092908.

20. Sun, Y.; Eller, B.S.; Nemanich, R.J.; J. Appl. Phys. 2011, 110, 084303-084309.

21. Carville, N.C.; Manzo, M.; Damm, S.; Castiella, M.; Collins, L.; Denning, D.; Weber, S.A.L.; Gallo, K.; Rice, J.H.; Rodriguez. B.J.; ACS Nano, 2012, 6, 7373–7380.

22. Schaufele, R.F.; Weber, M.J.; Phys. Rev. 1966, 152, 705–708.

23. Kim, K.; Shin, D.; Choi, J.Y.; Kim, K.L.; Shin, K.S.; J. Phys. Chem. C, 2011, 115 24960-24965.

24. Wu, D.; Liu, X.; Huang, Y.; Ren, B.; Xu, X.; Tian, Z.; J. Phys. Chem. C, 2009, 113, 18212–18222.

25. Fang, Y.; Li, Y.; Xu, H.; Sun, M.; Langmuir, 2012, 26, 7737–7746.

26. Huang, Y.; Zhu, H.; Liu, G.; Wu, D.; Ren, B.; Tian, Z.; J. Am. Chem. Soc., 2010, 132, 9244–9246.

27. P. B. Johnson, R. W. Christy, Phys. Rev. B 6, 4370–4379 (1972)

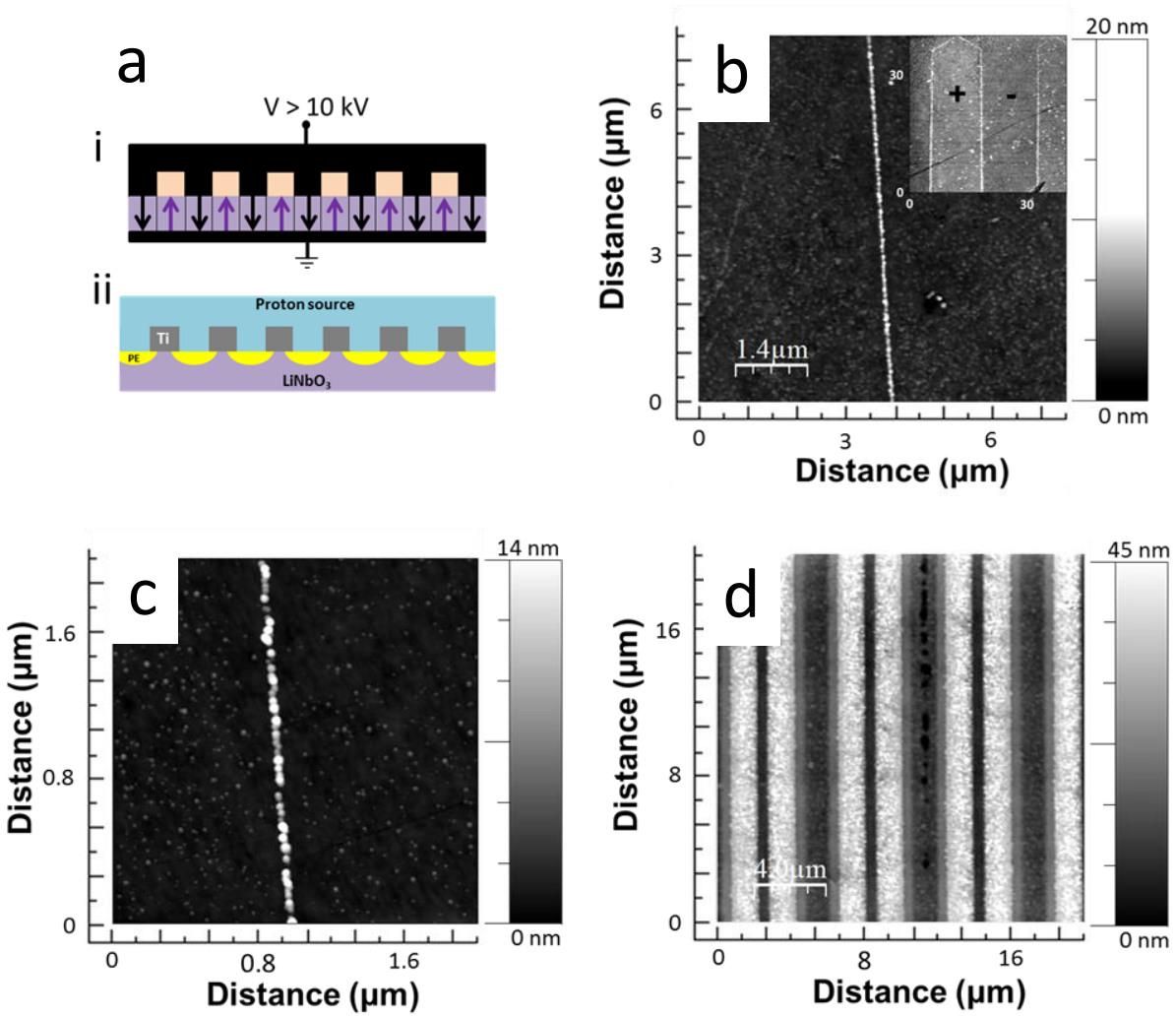

Figure 1. a) Schematic 2D cross-sectional structure of the i) periodic poled lithium niobate (PPLN) the black areas represent electrodes trough which voltage is applied to the already upward poled $LiNbO_3$ (purple). The pink blocks represent insulating material acting as a mask. Silver was mainly deposited along the boundaries between different polarizations, creating nanopatterned arrays along the x-axis. ii) $LiNbO_3$ with a Ti-mask emerged in a proton source (i.e. PPE methodology). Chemical processing of $LiNbO_3$ occuriured where the proton source could interact with $LiNbO_3$, causing Li+ to be replaced with H+. Silver deposited in the diffusion region below the mask, and mainly at the PE – $LiNbO_3$ boundary. b) AFM topography image showing linear arrangements (nanopatterns) of silver nanoparticles c.a. 10 nm in height and 200 nm in width on a PPLN sample. The insert shows

the terminal of the nanopattern, showing that two nanopatterns joining and is marked to show the +Z and –Z polled surfaces. c) Zoomed-in image showing the nanopatterns of silver nanoparticles from b). The insert is the PFM phase with a scan area of 8 μm and a data scale of 360^{o}. d) AFM topography image showing the nanopattern of silver nanoparticles on the PPE sample. The inset shows the different regions on the PPE surface, the $LiNbO_3$, lateral diffusion and PE-RIE region.

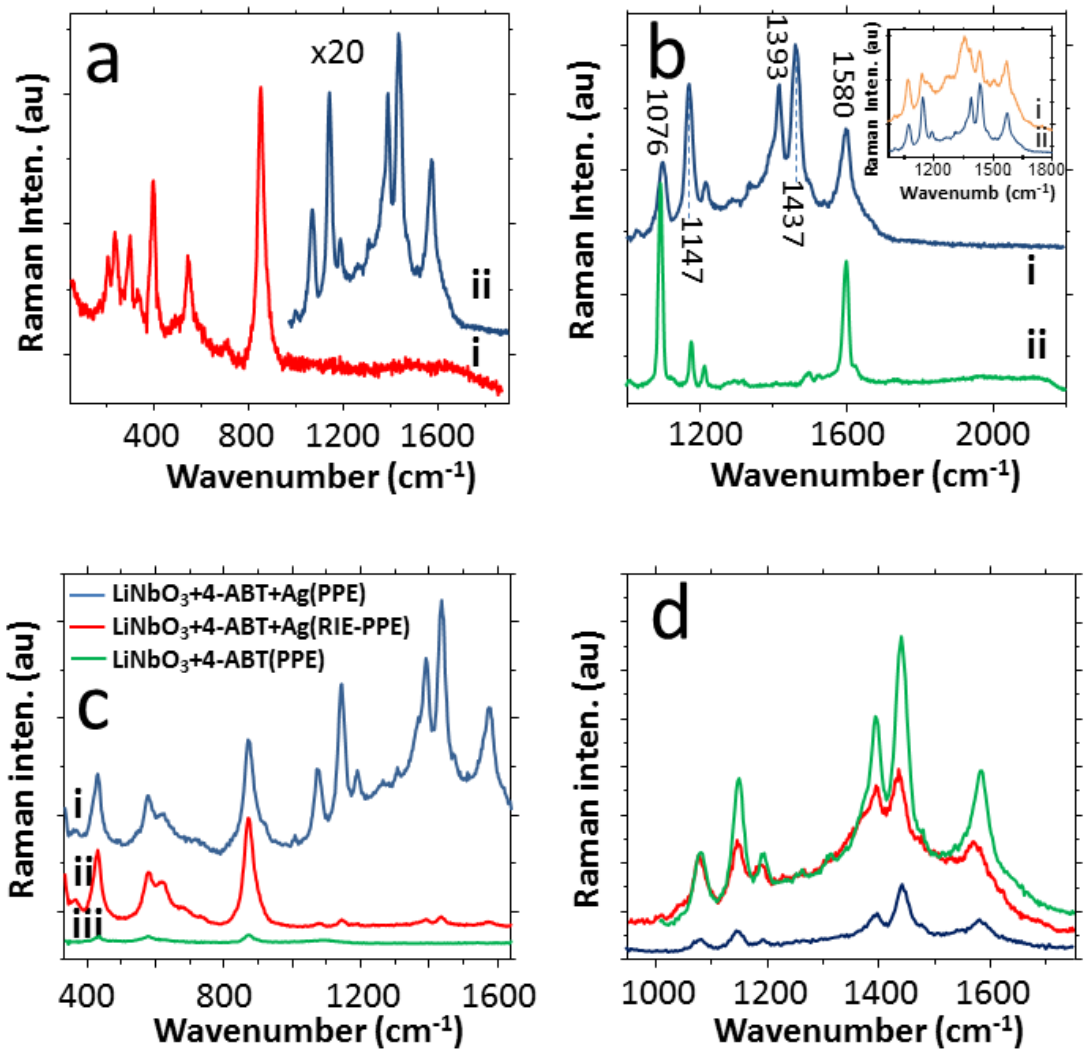

Figure 2. a) and b) shows the Raman spectra obtained using PPLN sample. a) i) Raman spectra of a substrate, $LiNbO_3$ + 4-ABT, ii) surface enhanced Raman of $LiNbO_3$ + Ag + 4-ABT λ_{ex} = 532 nm. b) i) Surface enhanced Raman spectra of $LiNbO_3$ + Ag + 4-ABT, λ_{ext} = 532 nm, ii) Raman spectrum of 4-ABT only, λ_{ext} = 532 nm. Insert shows surface enhanced Raman spectra of $LiNbO_3$ + Ag + 4-ABT recorded at λ_{ext} = i) 632 nm, ii) 532 nm. c) shows the Raman spectra obtained using the PPE sample recorded at λ_{ext} = 532 nm. Raman spectra of a substrate, $LiNbO_3$ + Ag + 4-ABT obtained at two different locations on the sample, On PPE (i) and RIE-PPE (ii) silver structures. (iii) show the Raman spectrum of a substrate, $LiNbO_3$ + 4-ABT on location of PPE silver structure. d) show the Raman spectra from a

substrate $LiNbO_3$ + Ag + 4-ABT on locations of PPE silver structures using three different excitation wavelengths, λ_{ext} = 532 nm (green graph), λ_{ext} = 633 nm (red graph) and λ_{ext} = 473 nm (blue graph).

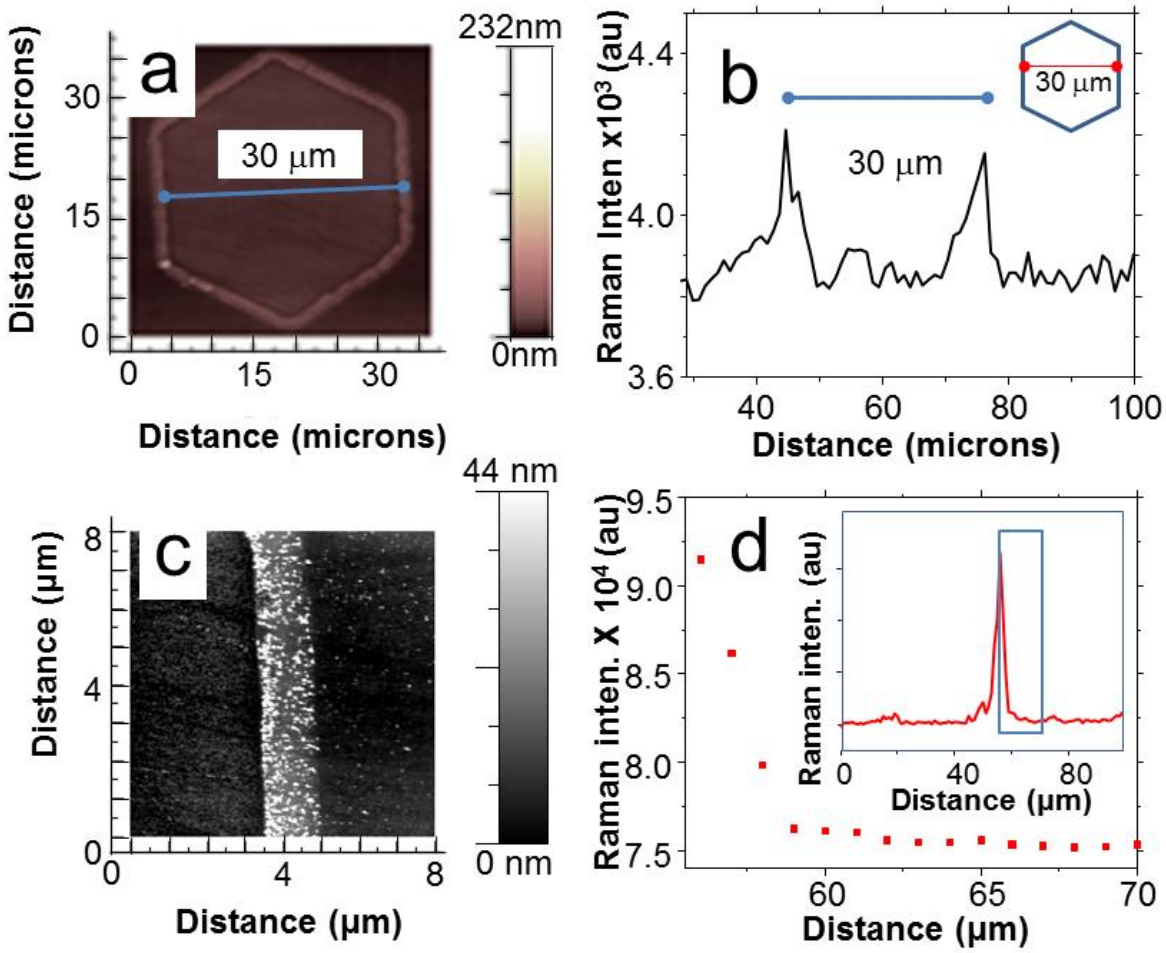

Figure 3. a) AFM topography image of a single hexagonal metallic structure, 30 µm in size b) a plot of Raman signal vs. distance obtained at the b_2 band (at 1160 cm^{-1}), inset shows a geometric drawing of the position of the line along which the measurements were taken. c) AFM topography image of the part of the 30 µm boundary in Figure a). d) Plot of Raman intensity vs. position across the domain proceeding from a position yielding the highest Raman signal of the b_2 band at 1437 cm^{-1}.

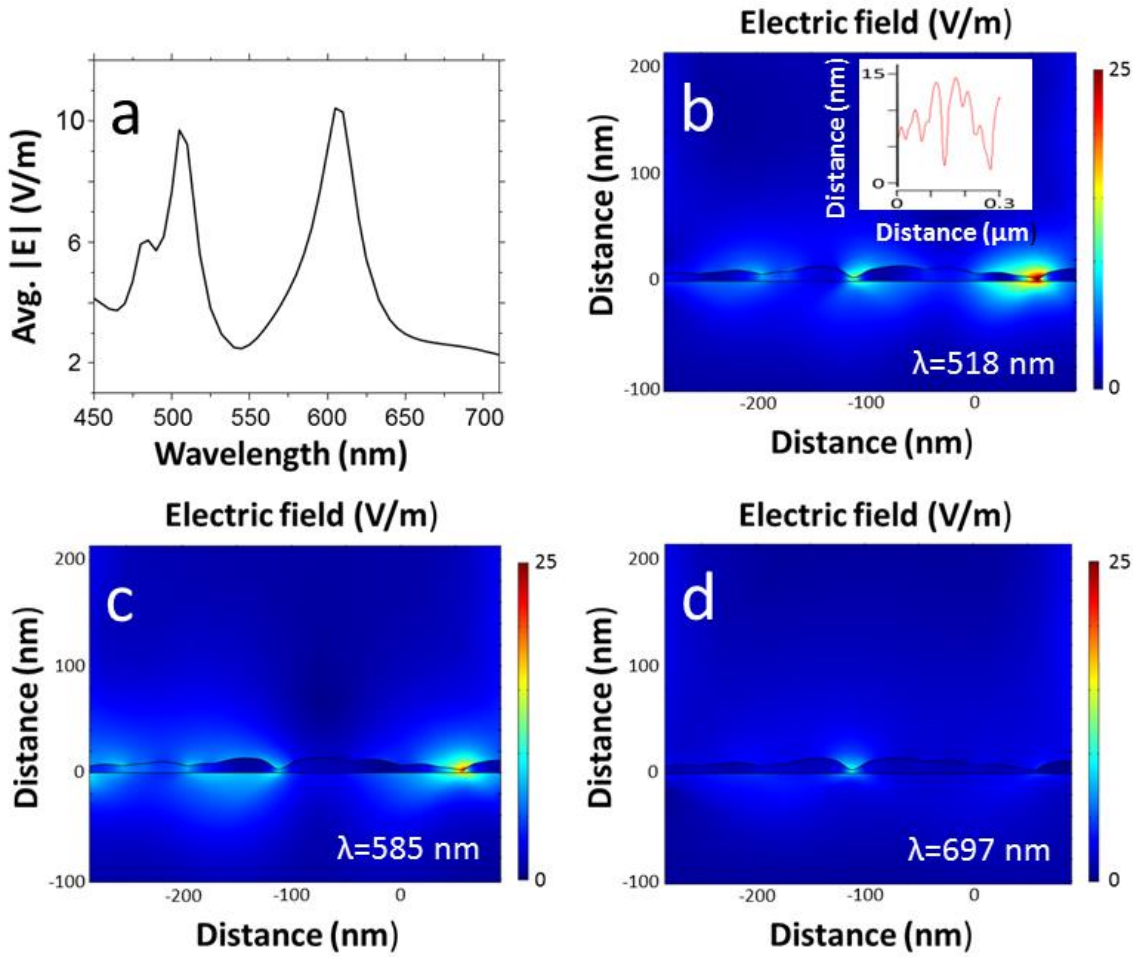

Figure 4. a) Shows the electric field measured at the bottom of the nanopattern spacing at different excitation wavelengths. b), c) and d) show the electric field distribution around a deep nanoparticle spacing along the PPLN silver nanopattern at wavelengths at which the scattered Raman signal from 4-ABT was detected for excitation wavelengths b) λ_{ext}=473nm , c) λ_{ext}=532 nm and d) λ_{ext}=633 nm. Inset in figure. 4b shows the AFM line profile obtained for the PPLN silver structure used in the COMSOL calculations.

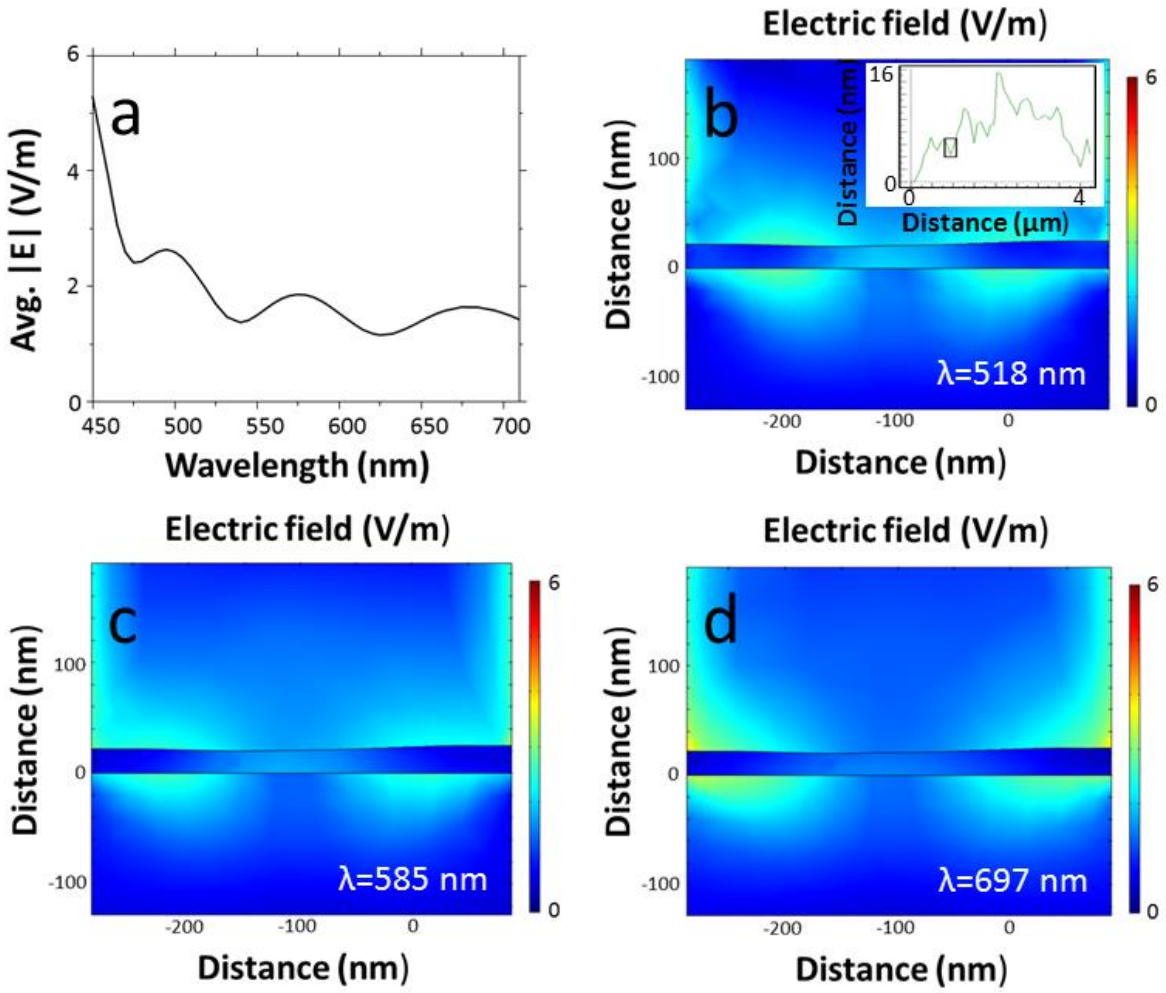

Figure 5. a) Shows the electric field measured at the bottom of the nanopattern spacing at different excitation wavelengths. b), c) and d) show the electric field distribution around a deep nanoparticle spacing along the PPE silver nanopattern at wavelengths at which the scattered Raman signal from 4-ABT was detected for excitation wavelengths b) λ_{ext}=473nm , c) λ_{ext}=532 nm and d) λ_{ext}=633 nm. a) Shows the electric field measured at the bottom of the nanopattern spacing at different excitation wavelengths. Inset in figure. 5b shows the AFM line profile obtained for the PPE silver structure. The area marked by a black box indicated the structure used in the COMSOL calculations.

Raman (cm^{-1}) Solid 4-ABT	SERS (cm^{-1}) PPLN + Ag + 4-ABT	SERS (cm^{-1}) PPE + Ag + 4-ABT	Vibrational assignment
1599(s)	1598 (w)	1598 (w)	ν_{CC} (a1)
	1580(s)	1576(s)	ν_{CC} (b2)
1496(w)	1487(w)	1473(w)	$\nu_{CC} + \delta_{CH}$ (a1)
	1437 (s)	1438 (s)	$\nu_{CC} + \delta_{CH}$ (b2)
	1393 (s)	1392 (s)	$\nu_{CC} + \delta_{CH}$ (b2)
	1309 (w)	1309 (w)	$\nu_{CC} + \delta_{CH}$ (b2)
1177 (w)	1193(w)	1191(w)	δ_{CH} (a1)
	1146(s)	1144(s)	δ_{CH} (b2)
1089 (s)	1076 (s)	1076 (s)	ν_{Cs} (a1)
1008 (w)	1006 (w)	1009 (w)	$\gamma_{CC} + \gamma_{CCC}$ (a1)

Table 1. Raman band positions taken from Figure 2 for Raman of solid 4-ABT and for SERS of 4-ABT on PPLN and PPE nanopatterns . Vibrational assignments are taken from ref 23.